Supplementary Information

Deep-Learning-Assisted High-Throughput Discovery of Metallophilic MA_2Z_4 Nanomaterials

Peng Zhang, Xiang Feng, Dominik Legut, Chao Lin, Haohao Dong, Zhihao Li, Zhi Wei Seh, Qianfan Zhang*

1. Exclusion of distorted adsorption systems

In this work, five criteria were established to exclude significantly distorted adsorption systems after structural relaxation. To control global structural distortions, adsorption systems were excluded if the total displacement of all atoms in the MA_2Z_4 slab (constructed as a 3 × 3 × 1 supercell of the primitive-cell MA_2Z_4) exceeded 5.0 Å during relaxation. Additionally, four criteria were devised to assess and restrict local structural distortions. Specifically, for each atom in the MA_2Z_4 atomic layers, if the in-plane displacement after relaxation exceeded 1.2 Å, the adsorption system was excluded. The layer thickness of each MA_2Z_4 atomic layer was also evaluated, and systems were discarded if the thickness exceeded 1 Å post-relaxation. For interlayer interactions, the out-of-plane separation between adjacent MA_2Z_4 layers, measured as the vertical distance between the nearest atoms in each layer, had to remain within the range of 0 to 3.4 Å, with systems exhibiting excessive separation or overlapping layers excluded. Furthermore, adsorption systems in which the adsorbed metal atom was found to reside beneath any MA_2Z_4 atomic layer after relaxation were removed. The critical thresholds for these criteria were determined through systematic testing, ensuring the retention of structurally stable or only slightly distorted adsorption systems while filtering out all configurations with pronounced distortions. Slightly distorted systems were deliberately retained to enhance the generalization and robustness of the machine learning model by allowing it to accommodate subtle structural variations in the dataset.

The critical distances mentioned earlier are determined through experimental testing. By applying these distances, the goal is to preserve as many adsorption systems as possible that are either undistorted or only mildly distorted, while effectively filtering out those with clear distortions. Retaining certain adsorption systems with minor distortions is intentional, as they can enhance the resilience of the machine learning (ML) model.

2. Details of the 336 features for each adsorption system

Here, we define the closest to the furthest MA_2Z_4 atom layers to the adsorbed metal atom as layer 1 to layer 7, respectively. For each layer, the interactions between the

adsorbed metal atom and the nearest 6 MA_2Z_4 atom groups are considered. Thus, the interactions between the adsorbed metal atom and a total of 42 MA_2Z_4 atom groups are considered. Then, we use 8 features to describe each interaction. As described in section 2.2, each feature has the formula |xm±xM|/dm-M, where xm and xM are the same kind of atomic properties of the metal atom and the MA_2Z_4 atom, respectively, and using plus sign or minus sign depend upon the characteristics of the atomic properties. Here, for the first 5 features, 5 kinds of atomic properties are adopted. Types of atomic properties and signs used in the formula are summarized is Table S1. For the 6th feature, we replace |xm ± xM| with constant 1, and the formula becomes 1/dm-M, which is an estimation of the interaction's distance. In this way, a total of 186 features are obtained for each adsorption system.

In this analysis, we designate the MA_2Z_4 atom layers from the one closest to the adsorbed metal atom to the furthest as layers 1 through 7, respectively. For each layer, the interaction between the adsorbed metal atom and the six nearest MA_2Z_4 atomic groups is evaluated, resulting in a total of 42 interactions considered for each adsorption system. Each of these interactions is characterized using eight features. As outlined in Section 2.2, the general formula for each feature is | xm ± xM |/d(m-M), xm and xM are the same kind of atomic properties of the metal atom and the MA_2Z_4 atom, respectively. The choice of the plus or minus sign in the formula depends on the specific nature of the atomic property. For the first five features, five distinct types of atomic properties are used, with their corresponding property types and signs detailed in Table S1. For the sixth feature, the term | xm ± xM | is replaced with a constant value of 1, simplifying the formula to 1/ d(m-M), which serves as an estimation of the interaction's distance. Altogether, this approach generates 186 features for each adsorption system, capturing detailed interaction characteristics.

Table S1. Types of atomic properties and the signs used in the feature formula.

Feature	Atomic property	Sign
1	Distance	Minus
2	Electronegativity	Minus
3	Atomic radius	Plus
4	Electron affinity	Minus
5	First ionization energy	Minus

6	Second ionization energy	Minus
7	Third ionization energy	Minus
8	Van der Waals radius	Plus

3. Details of the high-throughput workflow (HTW) and the MTL-CGCNN model

Step 1. Construction of initial structures. From a compositional space comprising 2,592 substrate materials, we randomly selected 400 candidates to construct initial structures using two distinct methods. For one hand, leveraging the experimentally validated crystal structure of $MoSi_2N_4$, we adjusted bond lengths by applying stretching ratios of 1.1, 1.3, and 1.5. This process generated initial structures for all 400 selected materials. For the other hand, bond lengths were set to 1.2 times the van der Waals radius of each atom. Additionally, interlayer angles along the z-direction between upper and lower atomic layers were defined as 45°, 55°, and 65°, creating alternative initial structures for each material. Following construction, these initial structures underwent multiple rounds of optimization. We extracted the energies of the optimized structures and compared them across both methods. For each substrate material, the structure exhibiting the lowest energy was designated as its stable configuration.

Step 2. Building a high-quality dataset and applying machine learning. Using the optimized structures from Step 1, we compiled a high-quality dataset by extracting key structural parameters, including lattice constants and three interlayer distances, to form the training set. The feature extraction methodology is detailed in the Supplementary Information (SI). We employed an Automated Machine Learning (Auto-ML) approach, which integrates numerous models to predict structural parameters with high precision via cross-validation. Testing revealed that initializing the remaining 2,196 substrate materials' structures with machine learning-predicted parameters reduced the number of ionic steps required for optimization by two-thirds. This significantly accelerated the Density Functional Theory (DFT) calculations. This process enabled us to construct and optimize the substrate structures across the entire compositional space, achieving a high convergence standard. Notably, our Auto-ML framework involved selecting over 100 machine learning models, weighted via Bayesian optimization, to produce an ensemble model. This ensemble, composed of multiple individual model contributions,

is well-documented in the literature for its robust energy prediction capabilities and widespread use in regression tasks within materials science.

Step 3. Construction of adsorption structures and dataset preparation. For the 2D material MA_2Z_4, we identified three high-symmetry surface sites as potential adsorption positions for single metal atoms. After extensive comparative analysis, an initial adsorption height of 2.5 Å was determined to be relatively stable and was used to construct initial adsorption structures. Across the entire compositional space, this yielded 62,208 initial adsorption structures. From this pool, we selected 2,310 structures for optimization. Of these, 1,697 met the convergence criteria and were incorporated into the training set. We then calculated their adsorption energy (E_b) and conducted statistical analysis to prepare a robust dataset for subsequent modeling.

Step 4. Framework design of the MTL-CGCNN model. The MTL-CGCNN model was developed by enhancing the existing Crystal Graph Convolutional Neural Network (CGCNN) framework. Key modifications included the incorporation of distance and Radial Basis Function (RBF) features and adjustments to the encoding of different material systems. These improvements enabled the model to better differentiate between material systems, facilitating accurate cross-system predictions of similar properties.

The database was labeled based on material_id, materials with id s≤1697 were assigned label 0 (representing MA_2Z_4 materials), while those with ids >1697 were assigned label 1 (representing MXene materials). This labeling inherently separates the dataset into two distinct groups with different crystal structures and compositions—MA_2Z_4 and MXene—prior to the split. The subsequent random splitting was performed within these predefined categories, ensuring that the structural differences between MA_2Z_4 and MXene materials are preserved across the training, validation, and test sets. This approach minimizes the risk of data leakage, as the split does not inadvertently mix structurally similar instances across sets. Additionally, we employed cross-validation to rigorously evaluate the splitting logic and confirm that the model's performance remains consistent across different splits. This step further ensures that the training, validation, and test sets are independent and identically distributed (i.i.d.)[1],

with no overlap between them.

Figure S1 provides a clear outline of the model's structure, from which we can derive the following information. The architecture of the model consists of several layers, each with specific parameters that contribute to the overall design. The embedding layer, which maps the input features into a lower-dimensional representation, has a total of 12,960 parameters and is defined by a size of [216]. Following this, the convolutional blocks, which apply N convolutional operations and include batch normalization (BN), contain the largest number of parameters, amounting to 1,544,400. These layers are responsible for extracting hierarchical feature representations from the input data. The pooling layer, with a size of [216] and 470,880 parameters, likely includes gated pooling mechanisms, which adaptively adjust how features are aggregated. Next, the fully connected layer, a typical multi-layer perceptron (MLP), connects the output of the pooling layer to the final output, with 235,440 parameters. Finally, the model outputs the predicted 2D material properties through a linear regression layer, which has 31,386 parameters. Overall, the model's architecture ensures a comprehensive process for feature extraction and prediction, with the convolutional blocks contributing the majority of the parameter count. The sizes of the layers in the figure are consistent with the parameter values described, reflecting a coherent design that integrates both the model's functional and structural components.

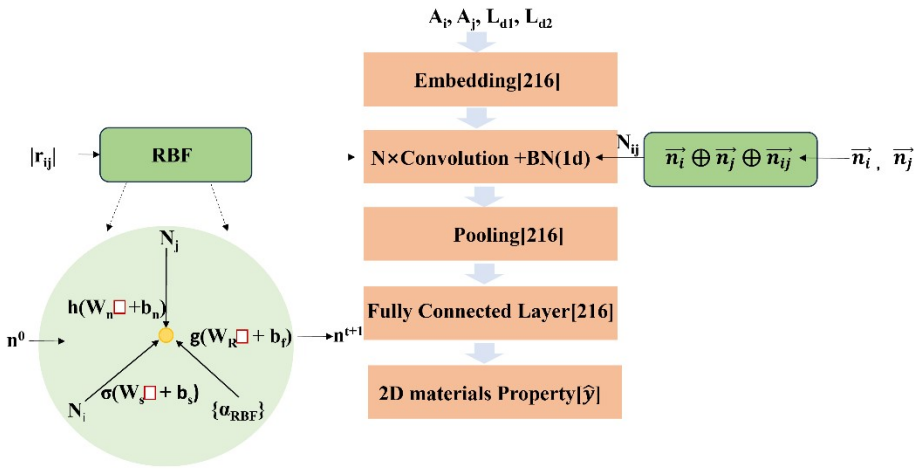

Figure S1. Schematic of the model MTL-CGCNN architecture.

4. Details of the Auto-ML model

Using the automated machine learning (Auto-ML) technique, a total of 632 ML

models (the model types include Adaboost regression, ARD regression, Decision tree regression, Extra trees regression, Gaussian process, Gradient boosting regression, K-nearest neighbor regression, Lib linear support vector regression, Support vector regression, Multiplayer perceptron, Random-forest regression, and Stochastic gradient descent regression) are evaluated during the Bayesian optimization process. We also employed the Bayes SearchCV[2] from scikit-optimize to define a search space for model weights, treating them as continuous hyperparameters within [0,1]. An objective function evaluates the ensemble's performance (e.g., cross-validated accuracy) by combining predictions from individual models (e.g., RandomForestClassifier[3], Gradient Boosting Classifier) weighted by these parameters. Bayesian optimization iteratively samples weight combinations, using a probabilistic model to focus on promising configurations, maximizing performance while minimizing computational cost. This approach efficiently balances the contributions of diverse models, enhancing the ensemble's predictive power. The top-6 models with the best performance are combined into an ensemble model as the final ML model used for binding strength (E_b) prediction. Also using the same feature extraction method, auto-ML predicted initial structural parameters that significantly reduced the computational cost of geometry optimizations. For a dataset of 400 primitive cell structures, initializing with Auto-ML-predicted parameters reduced the number of ionic steps required for convergence by approximately two-thirds compared to random initialization. This reduction underscores Auto-ML’s effectiveness in providing reasonable starting points for structural optimization, a simpler task than predicting complex properties like adsorption energy (Figure S2).

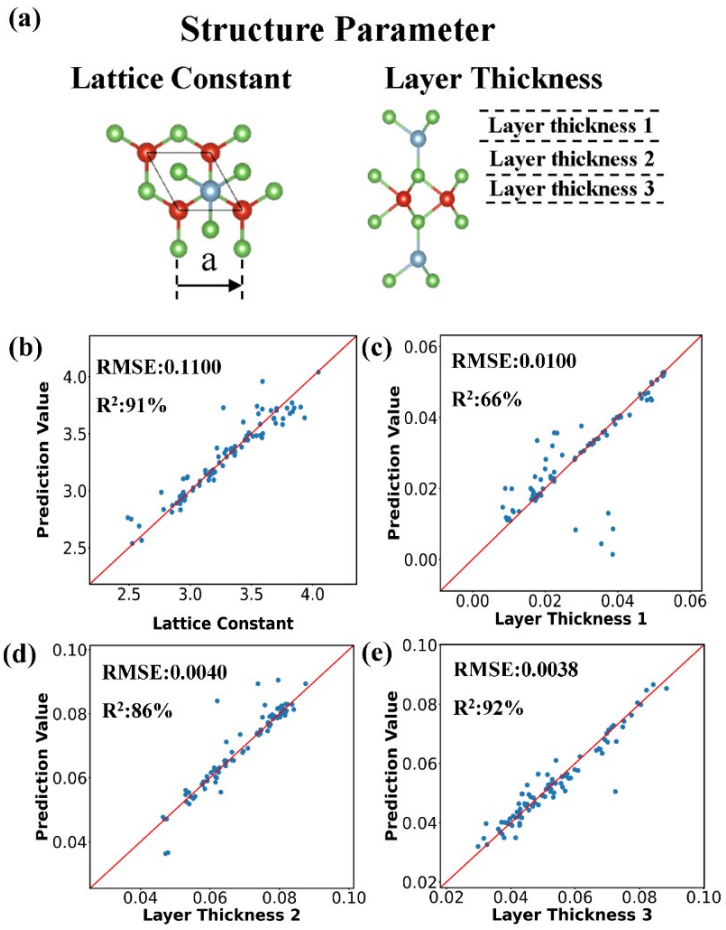

Figure S2. Prediction of material structural parameters using the Auto-ML model. (a) Schematic representation showing structural parameters including lattice constant and layer thickness. Comparison of predicted and actual values for (b) the lattice constant. Predicted vs. actual values for (c) layer thickness 1, (d) layer thickness 2, and (e) layer thickness 3, respectively, with corresponding RMSE and R^2 value shown.

5. Results of MTL-CGCNN model and baseline models

The provided bar chart compares the performance of three models—CGCNN, MTL-CGCNN, and Auto-ML—in predicting adsorption energy, evaluated using Mean Absolute Error (MAE) and Root Mean Square Error (RMSE). The 95% confidence intervals (CIs) and p-values from significance tests are critical for validating the claimed improvements (Figure S3).

For MAE, the mean values are 0.470 (CI: [0.4670, 0.4734]) for CGCNN, 0.420 (CI: [0.4178, 0.4230]) for MTL-CGCNN, and 0.650 (CI: [0.6469, 0.6539]) for Auto-ML. The narrow CIs indicate stable performance across multiple experiments, while

the non-overlapping intervals suggest significant differences. The p-value of 7.00E-10 confirms that these differences are highly statistically significant, with MTL-CGCNN outperforming CGCNN (the SOTA baseline method). For RMSE, the mean values are 0.778 (CI: [0.7764, 0.7828]) for CGCNN, 0.769 (CI: [0.7670, 0.7726]) for MTL-CGCNN, and 1.100 (CI: [1.0959, 1.1037]) for Auto-ML. Similarly, the tight CIs reflect consistency, and the lack of overlap, especially with Auto-ML, indicates notable performance gaps. The p-value of 2.30E-04 further supports the statistical significance of these differences, reinforcing MTL-CGCNN's slight edge over CGCNN.

These results demonstrate that MTL-CGCNN provides the most accurate and reliable predictions for adsorption energy, supported by both the confidence intervals and significance tests. The inclusion of these statistical measures validates the claimed improvements, ensuring the findings are robust and not due to random variation.

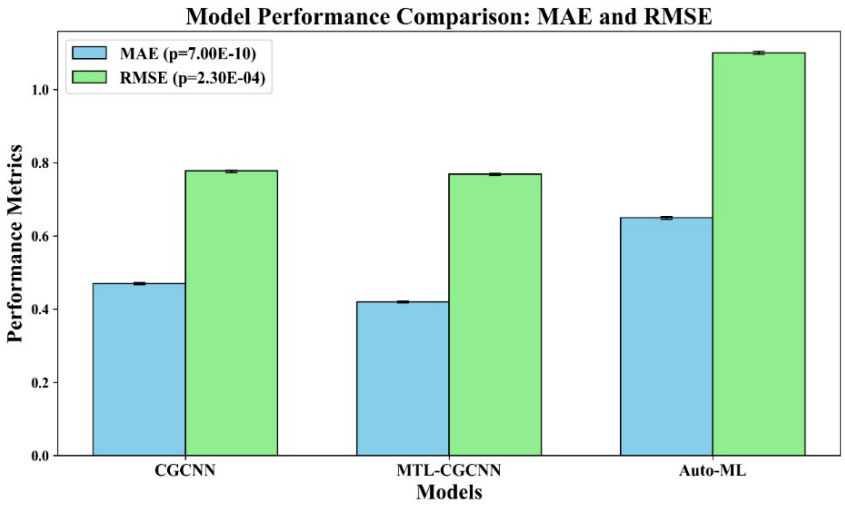

Figure S3. Confidence intervals and significance tests.

Based on our dataset, we compared four models for material property prediction such as MTL-CGCNN (multi-task learning, efficient label integration), Geo-CGCNN (EGAT-based, geometric focus), BE-CGCNN (one-hot encoding, system-specific), and CrysCo (transformer-based, self-attention). Based on the results in Table S2, the models' performance can be evaluated in terms of prediction accuracy (MAE) and generalization capability (R^2). MTL-CGCNN outperforms all other models with the lowest MAE of 0.42 eV, indicating its superior prediction accuracy. Additionally, it achieves the highest R^2 value of 0.90, demonstrating excellent generalization ability,

even for extreme values. In comparison, Geo-CGCNN ranks second with an MAE of 0.58 eV and an R^2 of 0.80, benefiting from its geometric focus on Voronoi tessellation and three-body correlations, though it still lags behind MTL-CGCNN in extreme value prediction. Crysco shows a slightly higher MAE of 0.77 eV and a lower R^2 of 0.75, struggling with large datasets and edge relationships. BE-CGCNN, with the highest MAE of 0.92 eV, is restricted to specific systems like Pt-O and Pt-OH, limiting its broader applicability and generalization across various datasets. The results highlight that MTL-CGCNN not only provides the best prediction accuracy but also excels in handling extreme values, outperforming the other models in both prediction and generalization capabilities.

Table S2. Prediction accuracy of different models.

Model	MAE (eV)	R^2 (Ordered Residuals vs Theoretical Quantiles)
BE-CGCNN	0.92	0.85
Geo-CGCNN	0.58	0.80
Crysco	0.77	0.75
MTL-CGCNN	0.42	0.90

The training process of MTL-CGCNN is the most stable, as shown in Figure S4d, with consistently low values of ΔMAE (Validation MAE - Training MAE) throughout the training epochs. This indicates minimal overfitting and a smooth convergence, demonstrating its robustness during training. In contrast, other models like Cryosco (Figure S4a) and BE-CGCNN (Figure S5a) exhibit more fluctuations in their ΔMAE curves, suggesting that their training processes are less stable, with higher variations between training and validation errors. Geo-CGCNN (Figure S5c) also experiences some instability, particularly in the later epochs. The superior stability of MTL-CGCNN likely contributes to its better generalization ability, as reflected in both its low MAE and high R^2 value.

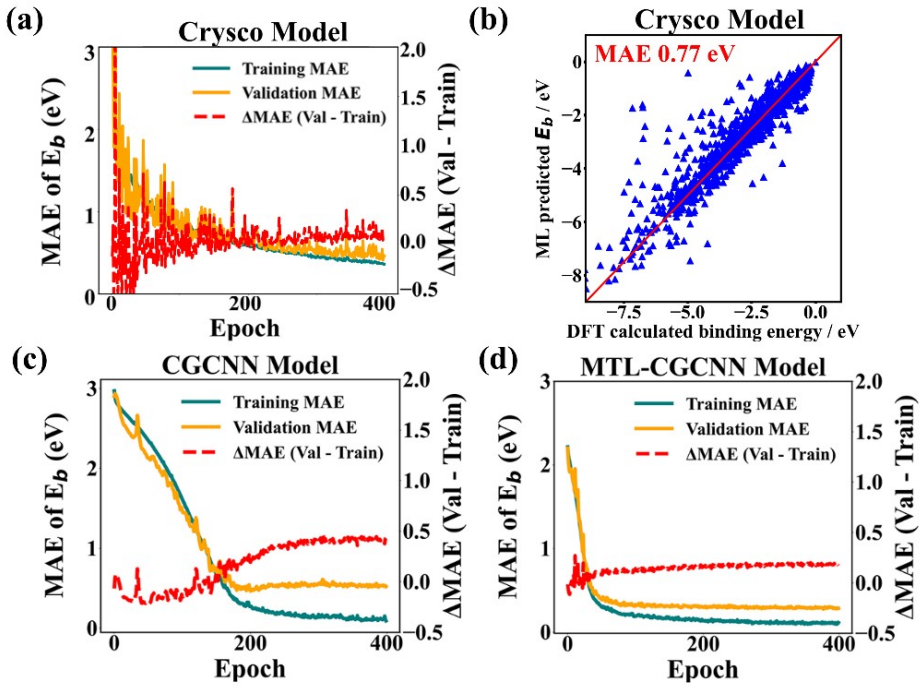

Figure S4. (a) Train process of Crysco model. (b) Prediction of Crysco model. (c) Train process of CGCNN model. (d) Train process of MTL-CGCNN.

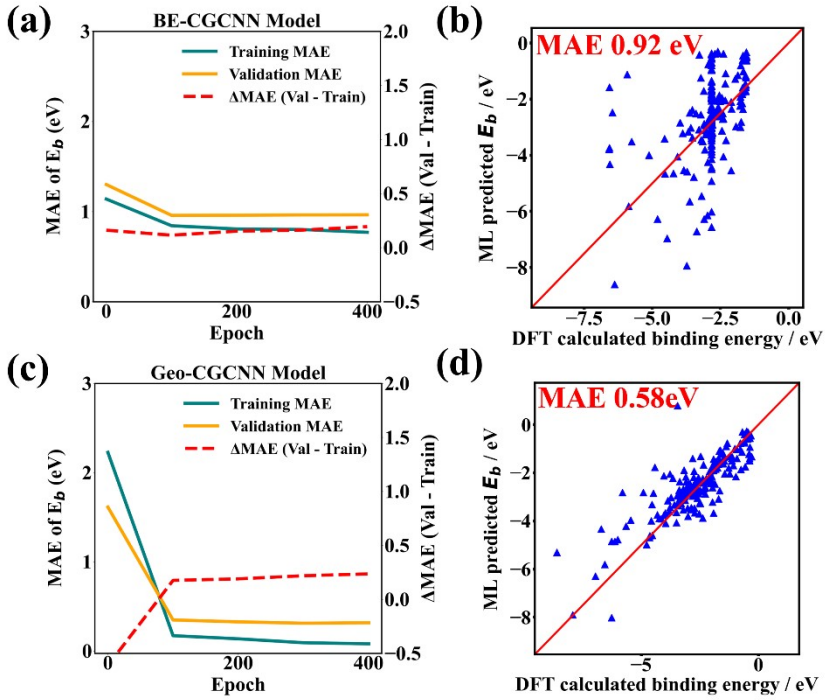

Figure S5. (a) Train process of BE-CGCNN model. (b) Prediction of BE-CGCNN model. (c) Train process of Geo-CGCNN model. (d) Prediction of Geo-CGCNN model.

The generalization capability of the MTL-CGCNN model is evidenced by the high R^2 fit between the actual and standard residual distributions, indicating strong

generalization performance (Table S2). The residual distribution can also be evaluated using a Quantile-Quantile Plot (Q-Q plot). The Q-Q plot compares the model's predicted residuals (Ordered Residuals) with the theoretical quantiles (Theoretical Quantiles). If the residual distribution follows a normal distribution, the red points (representing residuals of low and medium quantile samples) should be as close as possible to the yellow line (the reference line for the theoretical normal distribution). Due to the low proportion of high quantile samples (high E_b values) in the training set, the model lacks sufficient samples to learn the distribution characteristics of these extreme values. Structures with high adsorption energy often involve complex atomic interactions or unstable chemical environments, which increase the difficulty of prediction. However, from Figure S6, it can be observed that the MTL-CGCNN model, the red points are close to the yellow line in most areas, and the deviation of the red points from the yellow line in the high quantile region is relatively small, indicating that the model's prediction residuals for high energy values are relatively small, and its prediction generalization ability is superior to the other two models. This is attributed to the advantages of multi-task learning, which enables the model to better capture the complex features of the material system.

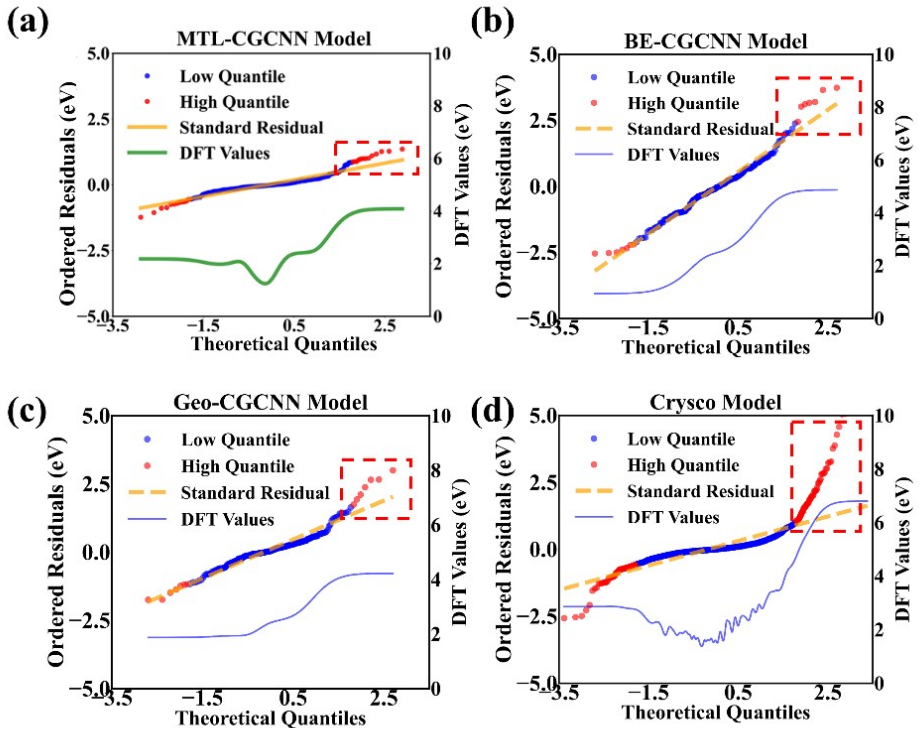

Figure S6. (a) Q-Q plot of MTL-CGCNN. (b) Q-Q plot of Beo-CGCNN model. (c) Q-

Q plot of Geo-CGCNN model. (d) Q-Q plot of Crysco model.

Besides, we provide additional comparison measurement for our method and base models (Table S3). MedAE is the median of the absolute differences between predicted and actual values. It indicates the "typical" error magnitude in model predictions. By using the median instead of the mean, MedAE is robust against outliers (such as exceptionally large or small errors), providing greater reliability. MAPE is the average of the absolute percentage differences between predicted and actual values. It represents the average relative magnitude of the prediction error compared to the actual values, aiding in the assessment of error proportion. MaxErr is the largest absolute error across all model predictions, illustrating the worst-case performance of the model's prediction.

Table S3. The variance of MAE and RMSE values in the three models.

Model	variance of MAE (10^{-6})	variance of RMSE (10^{-6})
CGCNN	5.36	5.44
MTL-CGCNN	6.24	7.76
Auto-ML	3.44	4.16

The difference we report a comprehensive set of evaluation metrics for our model on the test set for database MAE=0.42, RMSE=0.77, MedAE=0.1913, R^2=0.8279, MAPE=15.33%, and MaxErr=5.4145. The difference between MAE (0.42) and RMSE (0.77) indicates variability in prediction errors, with larger errors contributing disproportionately to the RMSE, suggesting occasional inconsistent predictions. The low MedAE (0.1913) shows that most predictions have small errors, but the high MaxErr (5.4145) highlights instances of significant deviations, reflecting performance variance. Additionally, the R^2 of 0.8279 indicates that 17.21% of the variance remains unexplained, contributing to prediction uncertainty, while the MAPE (15.33%) quantifies relative error magnitude. These metrics collectively provide a robust assessment of both variance and uncertainty, and we have added a discussion of these aspects to the revised manuscript to better inform readers about the model's reliability and limitations.

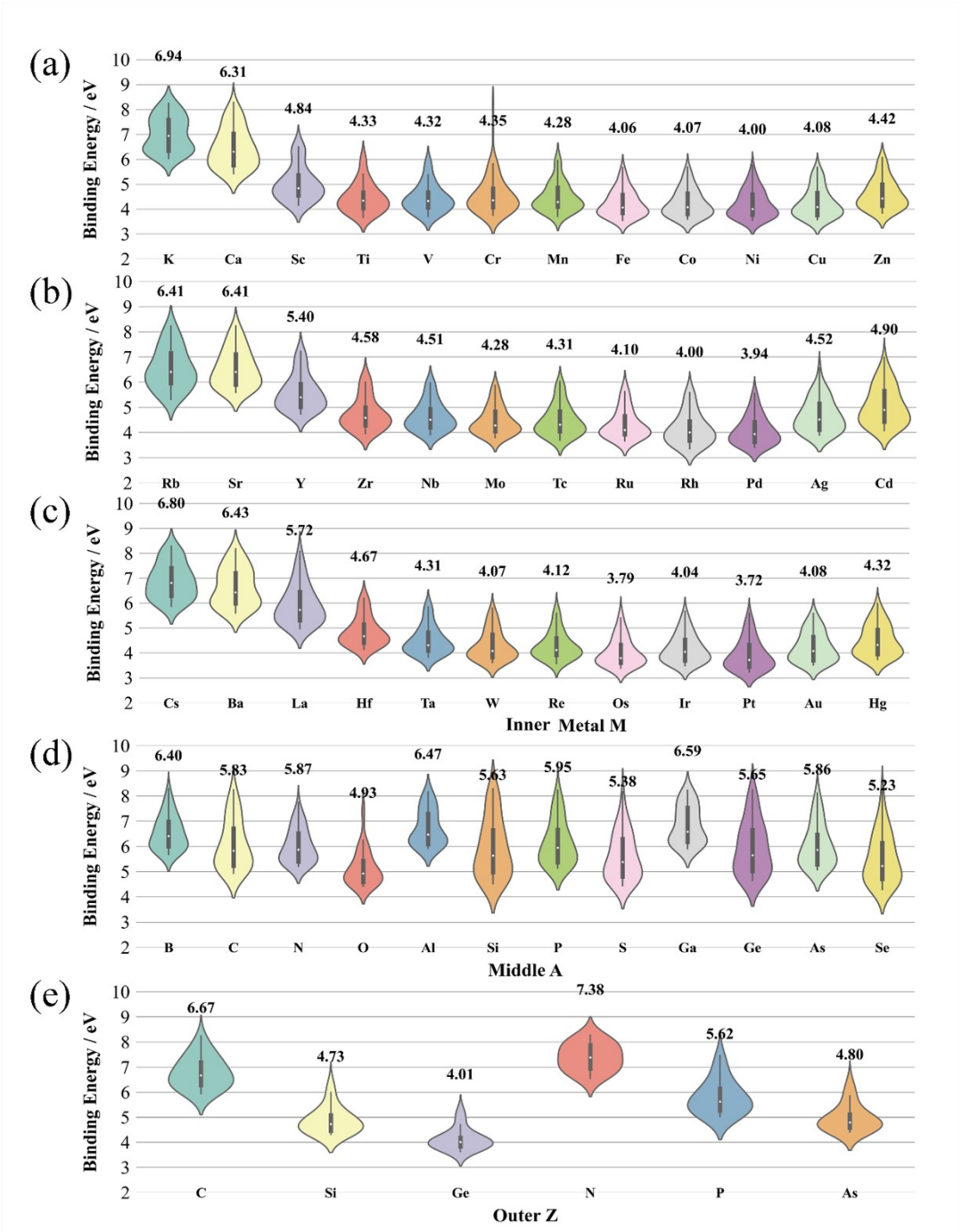

Figure S7. Violin plots of binding energy distributions for MA_2Z_4 configurations for different elements (periods) of the Periodic Table. (a-c) Inner metals M. (d) Middle elements A. (e) Outer elements Z.

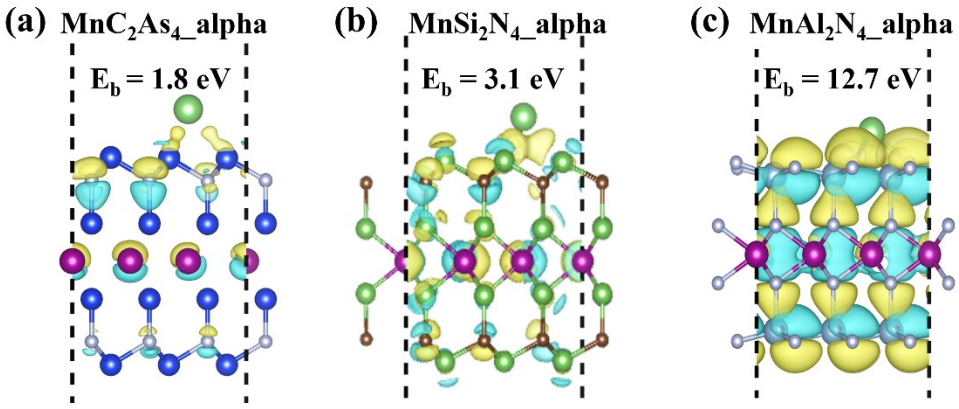

Figure S8. Charge density plots corresponding to structures with high to low adsorption energy. (a) MnC_2As_4_alpha. (b) $MnSi_2N_4$_alpha. (c) $MnAl_2N_4$_alpha.

5. Phonon spectra and electronic bands of MA_2Z_4 with the strongest metallophilicity

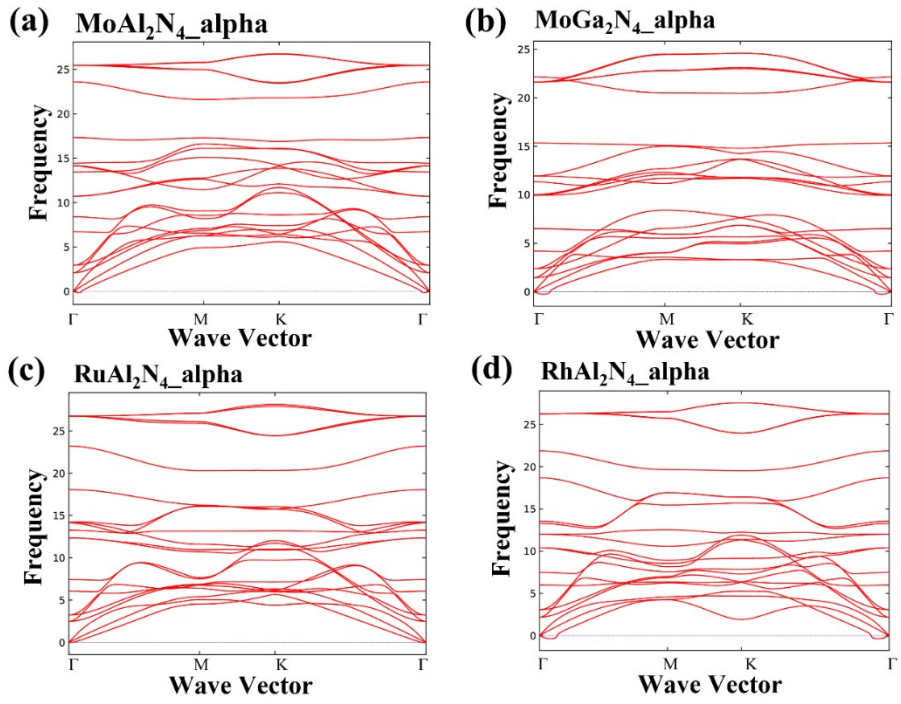

Figure S9. Phonon spectrum corresponding to the four structures with the highest adsorption energy. (a) $MoAl_2N_4$_alpha. (b) $MoGa_2N_4$_alpha. (c) $RuAl_2N_4$_alpha. (d) $RhAl_2N_4$_alpha.

6. Charge Transfer Amount vs. Adsorption Energy plots of MA_2Z_4

Here is the introduction in English based on the scatter plots depicting the relationship between Bader charge transfer and adsorption energy for eight metal atoms adsorbed on MA_2Z_4 surfaces. The scatter plots illustrate the correlation between Bader charge transfer and adsorption energy for eight metal atoms (Li, Na, K, Ca, Mg, Fe, Zn,

and Al) adsorbed on MA_2Z_4 surfaces, fitted with a unified second-degree polynomial. Divalent metals (Ca, Mg, Zn) exhibit the strongest correlation, with R^2 values exceeding 50% (0.58, 0.64, and 0.50, respectively), while monovalent metals (Li, Na, K) and trivalent metals (Fe, Al) show weaker correlations, with R^2 values around 20% (0.24, 0.19, 0.19, 0.23, and 0.36, respectively), highlighting the influence of metal valence on this relationship.

This correlation provides evidence for the role of electronegativity differences in determining adsorption energy. The stronger relationship for divalent metals suggests that their electronegativity difference with the MA_2Z_4 surface drives more consistent charge transfer, directly enhancing adsorption strength, whereas the weaker correlations for monovalent and trivalent metals indicate that additional factors may dilute this effect.

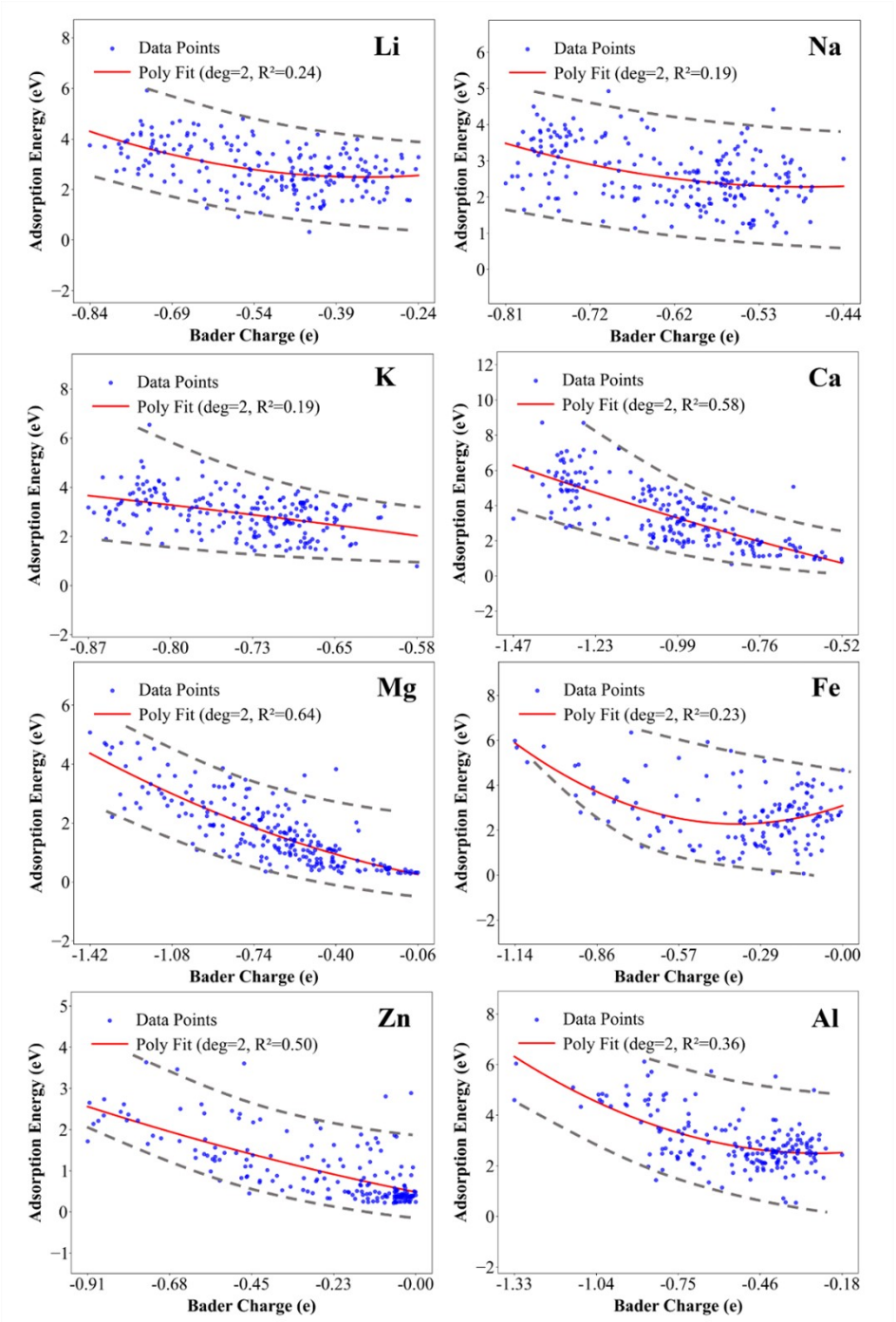

Figure S10. Relationship between charge transfer amount and adsorption energy for eight metal atoms.

7. The mechanical properties of the screened candidates MA_2Z_4

To facilitate experimental validation, our machine learning workflow screened 2,592 MA_2Z_4 materials, identifying 862 candidates with no imaginary frequencies in their phonon spectra and dynamic stability, ensuring their potential for practical synthesis and application (Figure S11). These materials were further evaluated based on key mechanical properties to ensure their suitability for practical applications.

To ensure their suitability for practical applications, we evaluated these materials based on key mechanical properties. These properties include in-plane Young's modulus (E_{xy})[4], which measures stiffness and resistance to deformation; out-of-plane shear modulus (G_z)[5], which indicates resistance to shear stress along the z-direction; and in-plane Poisson's ratio (μ_{xy}), which describes lateral deformation under tensile or compressive stress, ensuring structural integrity and stress absorption. Additionally, elastic stability confirms mechanical reliability under typical stress conditions, serving as a critical metric for practical utility.

To guide experimental synthesis, we established stringent criteria to prioritize candidates. We selected materials with an in-plane Young's modulus (E_{xy})[4] greater than 200 GPa, preferably exceeding 300 GPa, which is comparable to or surpasses MoS_2 (270–330 GPa), indicating high stiffness and deformation resistance. We also required a shear modulus (G_z)[6] greater than 50 GPa, with some candidates approaching 280 GPa, even exceeding graphene's shear modulus, ensuring excellent resistance to shear deformation and potential to prevent metal dendrite penetration. Furthermore, we targeted a Poisson's ratio (μ_{xy}) between 0.2 and 0.5[7,8], aligning with materials like MoS_2 (0.25–0.3) and h-BN (0.21–0.25), which ensures moderate lateral deformability. Based on these criteria, we identified 50 thermodynamically stable materials with superior mechanical properties, corresponding to dataset indices 5, 6, 12, 13, 14, 22, 23, 27, 30, 34, 45, 49, 59, 61, 69, 75, 76, 77, 81, 82, 85, 89, 90, 97, 99, 100, 104, 111, 122, 126, 131, 146, 147, 152, 153, 168, 173, 180, 181, 182, 184, 187, 189, 196, 201, 204, 213, 214, 229, 231, 233, 234, 242, 247, 253, 270, 273, 279, 298, 301, 310, 318, 326, 342, 343, 349, 354, 359, 375, 390, 395, 405, 417, 421, 422, 426, 436, 437, 440, 449, 451, 453, 454, 464, 468, 470, 475, 480, 488, 497, 505, 506, 511, 512, 522, and 537.

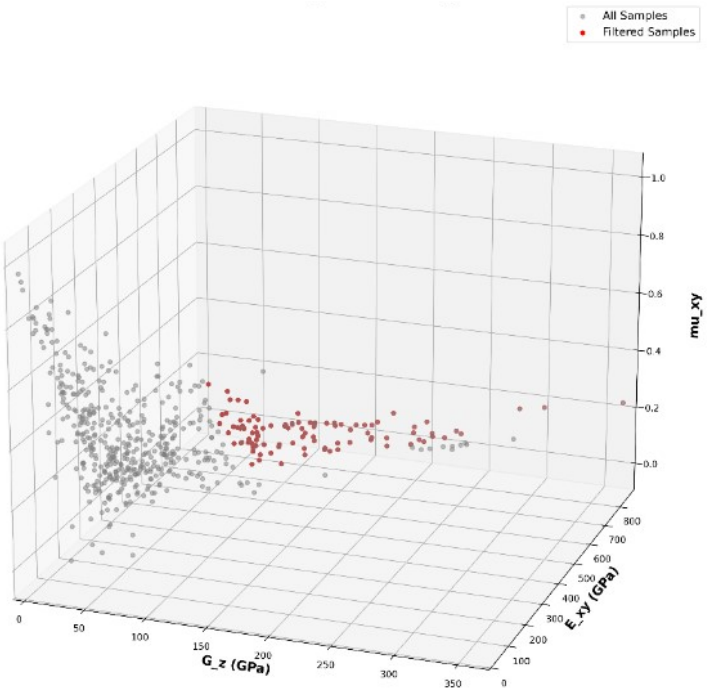

Figure S11. Schematic diagram of the mechanical properties of MA_2Z_4 materials.

To enhance the experimental relevance of our findings, we recommend prioritizing the synthesis of these 50 materials, particularly those with exceptional properties for specific applications. Notably, $MoAl_2N_4$ (alpha) stands out due to its outstanding mechanical properties and high adsorption energy (Figure S12).

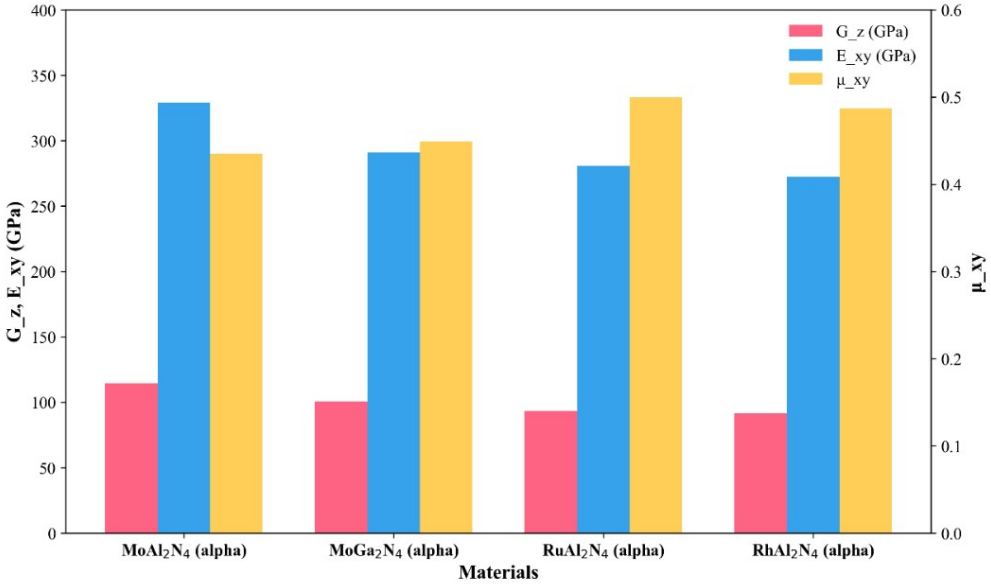

Figure S12. Mechanical properties of materials with the highest adsorption energy.

Reference

1 1 Q. An, S. Rahman, J. Zhou and J. J. Kang, 2023, **23**, 4178.
2 2 J. Bergstra and Y. Bengio, 2012, **13**, 281–305.
3 3 J. H. J. A. o. s. Friedman, 2001, 1189-1232.
4 4 S. Bertolazzi, J. Brivio and A. Kis, *ACS Nano*, 2011, **5**, 9703-9709.
5 5 S. H. Zhang and R. F. Zhang, *Computer Physics Communications*, 2017, **220**, 403-416.
6 6 C. Lee, X. Wei, J. W. Kysar and J. Hone, 2008, **321**, 385-388.
7 7 F. Liu, P. Ming and J. Li, *Phys. Rev. B*, 2007, **76**, 064120.
8 8 K. S. Novoselov, A. Mishchenko, A. Carvalho and A. H. Castro Neto, 2016, **353**, aac9439.

9